Preparation of Au-BiVO4 heterogeneous nanostructures as highly efficient visible-light photocatalysts

Cao, Shao-Wen; Yin, Zhen; Barber, James; Boey, Freddy Yin Chiang; Loo, Say Chye Joachim; Xue, Can

2011

Cao, S. W., Yin, Z., Barber, J., Boey, F. Y. C., Loo, S. C. J., & Xue, C. (2012). Preparation of Au-BiVO4 heterogeneous nanostructures as highly efficient visible-light photocatalysts. ACS applied materials & interfaces , 4(1), 418–423.

https://hdl.handle.net/10356/99790

https://doi.org/10.1021/am201481b

Preparation of Au-$BiVO_4$ Heterogeneous Nanostructures as Highly Efficient Visible-light Photocatalysts

Shao-Wen Cao,[†] *Zhen Yin,*[†] *James Barber,*[†,‡,§] *Freddy Y. C. Boey,*[†] *Say Chye Joachim Loo,*[*,†] *and Can Xue*[*,†]

[†]Solar Fuels Laboratory, School of Materials Science and Engineering, Nanyang Technological University, 50 Nanyang Avenue, Singapore 639798 (Singapore)

[‡]Division of Molecular Biosciences, Imperial College London, South Kensington Campus London SW7 2AZ, U.K.

[§]BioSolar Laboratory, Department of Material Sciences and Chemical Engineering, Polytechnic of Torino, Corso Duca degli Abruzzi, 24, 10129 Torino, Italy

*Corresponding Author. E-mail: cxue@ntu.edu.sg; joachimloo@ntu.edu.sg

ABSTRACT

Au-$BiVO_4$ heterogeneous nanostructures have been successfully prepared through in-situ growth of gold nanoparticles on $BiVO_4$ microtubes and nanosheets via a cysteine-linking strategy. The experimental results reveal that these Au-$BiVO_4$ heterogeneous nanostructures exhibit much higher visible-light photocatalytic activities than the individual $BiVO_4$ microtubes and nanosheets for both dye degradation and water oxidation. The enhanced photocatalytic efficiencies are attributed to the charge transfer from $BiVO_4$ to the attached gold nanoparticles as well as their surface plasmon resonance (SPR) absorption. These new hetero-nanostructures are expected to show considerable potential applications in solar-driven waste water treatment and water splitting.

KEYWORDS: electron transfer, heterojunction, photocatalyst, water splitting, surface plasmon resonance

INTRODUCTION

The increasing environmental problems and deficiencies of sustainable energy sources have driven considerable research efforts on photocatalytic pollutant degradation and water splitting by using visible light that is abundant in the solar spectrum. Many metal oxide semiconductors such as $BiVO_4$,[1,2] Bi_2O_3,[3,4] WO_3,[5,6] Fe_2O_3,[7,8] and Cu_2O[9,10] have been developed as photocatalysts with visible light activities. Among them, m-$BiVO_4$ with a band gap of E_g~2.40 eV has been recognized as a potentially suitable visible-light photocatalyst for pollutant decomposition and water oxidation.[11] Therefore, m-$BiVO_4$ with various morphologies, such as hierarchical nanostructures,[12] quantum tubes,[13] nanosheets,[14] nanoparticles,[15] microtubes,[16] and hollow structures,[17] have been synthesized by different methods and explored for photocatalytic reactions. These reported results indicate that the photocatalytic efficiencies of m-$BiVO_4$ are strongly dependent on its morphology and crystal phase. In addition, researchers have realized that the photocatalytic activity of $BiVO_4$ is usually not satisfied because the photogenerated active electrons and holes tend to rapidly decay through recombination,[18] which significantly restricted the practical applications of $BiVO_4$ in photocatalysis.

It has been reported that semiconductor photocatalysts loaded with noble metals, such as gold and silver, can effectively promote their photocatalytic performance because the charge transfer between the semiconductor and metal substantially improves the electron-hole separation, and the surface plasmon resonance (SPR) of the loaded metal nanoparticles provide additional visible light absorption which can also contribute to the overall photocatalytic activities.[19-28] Herein we report the preparation of Au-$BiVO_4$ heterogeneous nanostructures by growing gold nanoparticles on pre-synthesized $BiVO_4$ microtubes and nanosheets through a cysteine-linking strategy. Significantly, these Au-$BiVO_4$ heterogeneous nanostructures exhibit much higher visible-light photocatalytic activities than the individual microtubes and nanosheets for both dye degradation and water oxidation. Furthermore, we have investigated the roles of gold nanoparticles and have discussed the photoinduced electronic interaction between gold and $BiVO_4$, in order to have in-depth understanding on the enhanced photocatalytic performance.

EXPERIMENTAL SECTION

Synthesis of $BiVO_4$ microtubes and nanosheets. The protocol is modified from a previously reported method for preparing $BiVO_4$ nanoplates.[11] Briefly, while stirring, 158 mg of $BiCl_3$ was initially dissolved in 50 mL ultrapure water to form a white suspension, followed by the addition of 59 mg of NH_4VO_3. Then different amount of 1 M aqueous ethanolamine solution (2.5 mL for microtubes, 0.3 mL for nanosheets) was added into the suspension. The resultant mixture was sealed in a 100 mL teflon-lined stainless-steel autoclave. The autoclave was heated to and maintained at 160 ºC for 12 hours, and allowed to cool to room temperature. A yellow powder was collected after centrifugation, washed with water repeatedly, and then dried in a vacuum oven.

Synthesis of Au-$BiVO_4$ heterogeneous nanostructures. Gold nanoparticles were grown on the $BiVO_4$ microtubes and nanosheets according to a modifed literature method on preparing Fe_3O_4/Au hybrid spheres.[29] Briefly, 60 mg of the as-prepared $BiVO_4$ powder was suspended in 20 mL ultrapure water followed by the addition of 5 mL aqueous solution of 0.01 M L-cysteine. The mixture was subjected to sonication for 30 minutes followed by the addition of 5 mL aqueous solution of 3 mM $HAuCl_4$. After vigorous stirring for another 30 minutes, 10 mL aqueous solution of 0.05 M L-ascorbic acid was quickly added into the solution. The reaction was allowed for rapid stirring for 3 hours. The products were separated via centrifugation, washed with water repeatedly, and dried in a vacuum oven. Subsequently UV/ozone cleaning was used to treat the powders to remove cysteine bound on the product surface.

Characterization. X-ray powder diffraction (XRD) patterns were recorded on a Shimadzu XRD-6000 X-ray diffractometer (Cu Kα source) at a scan rate of 1 °/min with the 2θ range from 15 to 60°. The field emission scanning electron microscopy (FESEM) images were taken with a JEOL JSM-6340F scanning electron microscope. Energy dispersive X-ray spectra (EDX) were taken with a JEOL JSM-7600F scanning electron microscope equipped with energy dispersive X-ray analysis system. Transmission electron microscopy (TEM) images and selected area electron diffraction (SAED) patterns were recorded on a JEOL JEM-2010 transmission electron microscope at an accelerating voltage of 200 kV.

UV–vis absorption spectra and diffuse reflectance spectra (DRS) were recorded on a Lambda 750 UV/Vis/NIR spectrophotometer (Perkin Elmer, USA).

Photocatalytic degradation of methyl orange. Methyl orange (MO) was used as a convenient photo-stable organic molecule to assay photochemical activity of Au-$BiVO_4$. The prepared Au-$BiVO_4$ heterogeneous nanostructures (10 mg) were dispersed into an aqueous solution (10 mL) of methyl orange (5 $mg{\cdot}L^{-1}$). The suspension was sonicated for 15 min followed by stirring in dark for 15 min to ensure an adsorption-desorption equilibrium prior to irradiation. The suspension was then irradiated while stirring by using a 300-W Xe lamp (MAX-302, Asahi Spectra, USA) coupled with a UV cut-off filter (λ > 420 nm). The initial and final reaction temperature for MO solution were measured as 28 ºC and 32 ºC, respectively. Samples for analysis were taken from the reaction suspension after different reaction time and centrifuged at 10,000 rpm for 5 min to remove the particles. The MO concentration from the upper clear solution was analyzed according to the absorption intensity at 463 nm in the measured UV-vis spectra.

Photocatalytic oxidation of water for O_2 generation. Typically, 5 mg of the prepared Au-$BiVO_4$ heterogeneous nanostructures were suspended in 15 mL aqueous solution of 5.33 mM $Na_2S_2O_8$. The suspension was purged with argon for 3 hours to drive away the residual oxygen before sealed in a quartz flask. The photocatalytic water oxidation was carried out by irradiating the suspension with a 300-W xenon lamp (MAX-302, Asahi Spectra, USA) coupled with a UV cut-off filter (λ > 420 nm). The initial and final reaction temperature for the reaction solution were measured as 28 ºC and 34 ºC, respectively. The gas product composition was analyzed every 30 min by an Agilent 7890A gas chromatograph (GC) with TCD detector.

RESULTS AND DISCUSSION

The prepared $BiVO_4$ samples are identified as monoclinic $BiVO_4$ through XRD analyses (JCPDS No. 83-1699) as shown in Figure 1. The SEM and TEM images (Figure 2) reveal that the sample prepared

with 2.5 mL solution of ethanolamine is composed of tubular microstructures (Figure 2a and b), while using 0.3 mL solution of ethanolamine leads to nanosheet formation (Figure 2c and d). Both SAED patterns of a single microtube (Figure 2b) and a single nanosheet (Figure 2d) reveal the single crystalline nature of these structures. The corresponding diffraction spots can be indexed as 200, 020 and 220 reflections, indicating the preferred (001) surface orientation of both microtubes and nanosheets. The growth of Au on the $BiVO_4$ surface is facilitated in the presence of L-cysteine which can bind to the $BiVO_4$ surface through its carboxylate group. When the gold salt precursor ($HAuCl_4$) is subsequently added and reduced, the produced gold atoms can be captured by the L-cysteine on the $BiVO_4$ surfaces through Au–S bonding.[30] These gold atoms then serve as the nucleation sites for further in-situ growth on $BiVO_4$ surfaces. The original morphologies of microtube and nanosheet are retained during the gold nanoparticle growth process, as shown in Figure 3b and d. The high-magnification TEM images (Figure S1a-c) reveal that many small gold nanoparticles with an average size of 7.2 (±1.3) nm are sticking on the surfaces of $BiVO_4$ microtubes and nanosheets. In comparison, the surfaces of the pure $BiVO_4$ microtubes and nanosheets are very smooth, as shown in Figure 3a and c. The EDX analysis (Figure 3e and f) further confirms the presence of gold on the nanostructures with an estimated gold content of 3.71 wt % and 3.50 wt % for Au-$BiVO_4$ microtubes and nanosheets, respectively. Indeed, this cysteine-linking strategy is superior for preparing Au-$BiVO_4$ heterogeneous nanostructures as compared with simply mixing pre-synthesized gold nanoparticles (Figure S2) with cysteine-modified $BiVO_4$ nanostructures. The latter did not result in the formation of heterogeneous Au-$BiVO_4$ structures (Figure S3).

The diffuse reflectance spectra of the prepared $BiVO_4$ and Au-$BiVO_4$ samples are shown in Figure 4. The band gaps estimated by extrapolating the linear region of a plot of the absorbance squared vs. energy[31] are 2.52, 2.51, 2.55 and 2.54 eV for $BiVO_4$ microtubes, Au-$BiVO_4$ microtubes, $BiVO_4$ nanosheets and Au-$BiVO_4$ nanosheets, respectively. Thus these samples have almost no difference in the bandgap energy. Note the SPR band of gold nanoparticles does not appear in the spectra though the TEM images clearly indicate their existence on the $BiVO_4$ surfaces. Such a gold SPR band has been

numerously observed in Au-TiO_2 heterostructures,[32-35] while in the heterogeneous Au-$BiVO_4$ structure presented here, the absence of Au SPR band may be due to the low concentration of gold nanoparticles, thus the spectrum feature of Au SPR may be overwhelmed by the absorption of $BiVO_4$ which also exhibits considerable absorption in the same spectral region.

The photocatalytic activities of the Au-$BiVO_4$ heterogeneous nanostructures were evaluated through MO degradation under visible-light (λ > 420 nm) irradiation. As an example, Figure 5a shows the absorption spectra of MO solution in the presence of Au-$BiVO_4$ nanosheets as a function of illumination time. The absorption peak at 463 nm decreases significantly over a period of tens of minutes, indicating a relatively fast degradation of MO molecules in solution. For comparison, pure $BiVO_4$ microtubes and nanosheets were also used for photocatalytic MO degradation under the same conditions. Figure 5b shows that after 50 min visible-light irradiation, the degradation percentage of MO in the presence of Au-$BiVO_4$ microtubes and nanosheets are 36% and nearly 100%, respectively. The corresponding MO degradation rates are normalized per gram photocatalyst as 3.6 $mg \cdot L^{-1} \cdot min^{-1}$ and 10 $mg \cdot L^{-1} \cdot min^{-1}$ for Au-$BiVO_4$ microtubes and nanosheets, respectively. While the pure $BiVO_4$ microtubes and nanosheets exhibit almost no activities for MO degradation even though they have some absorption in the visible region, which excludes the MO self-degradation originated from dye-sensitization effect. The lower efficiency of Au-$BiVO_4$ microtubes than Au-$BiVO_4$ nanosheets might be partially due to the smaller light absorption cross-section of microtubes arising from the curved surface. Another reason could be because the absorption of gold nanoparticles attached on the inner surface of $BiVO_4$ microtubes is blocked by the tube wall so that these gold particles can not be excited to contribute SPR-enhancement. In contrast, the gold particles on the two sides of $BiVO_4$ nanosheets have equal opportunities to receive excitation. Nevertheless, our results still demonstrate that the deposited gold nanoparticles endow greatly enhanced visible-light photocatalytic efficiency.

We further compare the visible light (λ>420 nm) activities of the Au-$BiVO_4$ heterogeneous nanosheets with pure $BiVO_4$ nanosheets for photocatalytic water oxidation in the presence of sacrificial electron acceptor $S_2O_8^{2-}$. As shown in Figure 6, the light induced O_2 evolution rate for Au-$BiVO_4$

nanosheets (5862 μmol·h^{-1}·g^{-1}) is more than three times higher than that of pure $BiVO_4$ nanosheets (1579 μmol·h^{-1}·g^{-1}). This further confirms the high visible-light photocatalytic efficiency of the Au-$BiVO_4$ heterogeneous nanostructures caused by the in-situ grown gold nanoparticles.

The gold-enhanced photocatalytic efficiencies are attributed to two aspects. First, the conjugated gold nanoparticles on $BiVO_4$ surfaces may act as electron sinks to retard the recombination of the photogenerated electrons and holes in $BiVO_4$ so as to improve the charge separation on its surfaces. It is known that the Fermi level of gold is 0.5 V (versus NHE),[28] which is lower than the conduction band (CB) edge of $BiVO_4$ (0 V versus NHE).[36] At the Au-$BiVO_4$ hetero-junction, the interactions between Au and $BiVO_4$ establish an interfacial charge equilibrium. When the $BiVO_4$ is excited by visible light with photon energy larger than the its band gap, electrons in the valance band (VB) are excited to the CB with simultaneous generation of holes in the VB. At the interface of Au and $BiVO_4$, the photogenerated electrons are distributed, and some of them transfer into the Au nanoparticle until new interfacial charge equilibrium is attained. The electron accumulation on Au increases the Fermi level (E_f) of the gold nanoparticle to more negative potentials (E_f^*) which is closer to the $BiVO_4$ conduction band. This energy alignment for the Au-$BiVO_4$ junction is shown in Figure 7. Such a charge transfer process enhances the separation of photogenerated electrons and holes and thereby increases their lifetime.[28,37] This is particularly important for photocatalytic water oxidation because it is slow as multi-electron processes with kinetic restraints.[38] As illustrated in Figure 7, when the photogenerated electrons transfer to the gold nanoparticle and reduce the adsorbed $S_2O_8^{2-}$ to SO_4^{2-} on the Au surface, the holes remain on $BiVO_4$ surface will have relatively longer lifetime to carry out the four-electron process of H_2O oxidation to O_2.

Second, the SPR of gold nanoparticles attached on $BiVO_4$ surfaces can also enhance the visible light photocatalytic efficiency. Although the spectra (Figure 4) did not show observable SPR peak of gold nanoparticles due to the low concentration of gold nanoparticles on $BiVO_4$ surface, the effect of SPR-driven enhancement may still contribute to the photocatalytic reaction. In order to clarify the possible involvement of gold SPR in the enhanced photocatalytic activity of Au-$BiVO_4$ structures, we prepared

Pt-$BiVO_4$ nanosheets (Figure S4a and b) through the same strategy (Pt content as 3.78 wt%, see supporting information for details) to compare their photocatalytic efficiency with Au-$BiVO_4$ nanosheets for MO degradation under light irradiation at 500 ± 20 nm. This wavelength range is accordance with the SPR band of normal gold nanoparticles, while Pt nanoparticles have no absorption within this range.

As shown in Figure 8, the Au-$BiVO_4$ nanosheets are quite active for photocatalytic MO degradation, while the pure $BiVO_4$ nanosheets and Pt-$BiVO_4$ nanosheets show no activity for MO degradation under irradiation at the same wavelength range. This indicates that the relatively weak absorption of $BiVO_4$ at 500 ± 20 nm does not induce obvious photocatalytic activity even with Pt as electron sink. This might be due to the very inefficient excitation by the photons with energy close to the band gap so that the recombination of photogenerated electrons and holes dominate.[39] However, the gold nanoparticles deposited on $BiVO_4$ nanosheets exhibit strong SPR at 500 ± 20 nm. It has been extensively demonstrated that the plasmon-exciton coupling can result in significant enhancement of charge separation.[40] Therefore, we believe that the gold SPR can enhance the electron-hole separation near the Au-$BiVO_4$ hetero-junction, and thus improve the photocatalytic efficiency of the Au-$BiVO_4$ heterogeneous nanostructures, which is also supported by our observations.

Indeed if we use fully visible light (λ> 420 nm) irradiation, the Pt-$BiVO_4$ nanosheets still exhibit certain photocatalytic activity for MO degradation (Figure S4c) even though pure $BiVO_4$ nanosheets show no activity (Figure 5). This means that the deposited metal nanoparticles as “electron sink” do contribute to the improved charge separation and photocatalytic activity. Since the Au-$BiVO_4$ nanosheets still show much higher activity than the Pt-$BiVO_4$ by comparing Figure 5 and Figure S4c, it indicates that the SPR excitation of Au nanoparticles would provide stronger enhancement on charge separation than the effect only from “electron sink”, especially when the excitation photon energy is low (visible light) and closely above the bandgap of $BiVO_4$.

CONCLUSIONS

In summary, Au-$BiVO_4$ heterogeneous nanostructures have been successfully prepared through in-situ growth of gold nanoparticles on $BiVO_4$ microtubes and nanosheets by using a cysteine-linking strategy. These Au-$BiVO_4$ heterogeneous nanostructures exhibit highly efficient visible-light-driven photocatalytic activities for dye degradation and water oxidation as compared to pure $BiVO_4$ microtubes and nanosheets. The improved photocatalytic efficiencies are attributed to the enhanced charge separation by the contacting gold nanoparticles, allowing the photogenerated electrons and holes to have sufficient time to participate the overall photocatalytic reactions. Further comparison with Pt-$BiVO_4$ indicates that the SPR absorption of gold nanoparticles on the Au-$BiVO_4$ nanostructures also has significant contribution to the visible light photocatalytic activities. We believe that our strategy of the hetero-structure synthesis involving tethered Au nanoparticles on a semiconductor surface and exploiting their SPR for enhancing photocatalytic activities can have considerable impact on the future development of highly efficient visible-light photocatalysts for organic pollutant degradation and water splitting.

ACKNOWLEDGMENT

The authors acknowledge financial support from NTU Start-Up Grant (SUG), NTU seed funding for Solar Fuels Laboratory, and CRP (NRF-CRP5-2009-04) from NRF Singapore.

Supporting Information Available. Experimental details and characterization data for compared samples, and additional HRTEM images for Au-$BiVO_4$ microtubes and nanosheets. This information is available free of charge via the Internet at http://pubs.acs.org/.

REFERENCES

1. Iwase, A.; Kudo, A. *J. Mater. Chem.* **2010**, *20*, 7536–7542.

2. Wang, D. G.; Jiang, H. F.; Zong, X.; Xu, Q.; Ma, Y.; Li, G. L.; Li, C. *Chem. Eur. J.* **2011**, *17*, 1275–1282.

3. Saison, T.; Chemin, N.; Chanéac, C.; Durupthy, O.; Ruaux, V.; Mariey, L.; Maugé, F.; Beaunier, P.; Jolivet, J.-P. *J. Phys. Chem. C* **2011**, *115*, 5657–5666.

4. Zhang, L. S.; Wang, W. Z.; Yang, J.; Chen, Z. G.; Zhang, W. Q.; Zhou, L.; Liu, S. W. *Appl. Catal. A: Gen.* **2006**, *308*, 105–110.

5. Chen, D.; Ye, J. H. *Adv. Funct. Mater.* **2008**, *18*, 1922–1928.

6. Arai, T.; Yanagida, M.; Konishi, Y.; Ikura, A.; Iwasaki, Y.; Sugihara, H.; Sayama, K. *Appl. Catal. B: Environ.* **2008**, *84*, 42–47.

7. Duret, A.; Grätzel, M. *J. Phys. Chem. B* **2005**, *109*, 17184–17191.

8. Xie, H.; Li, Y. Z.; Jin, S. F.; Han, J. J.; Zhao, X. J. *J. Phys. Chem. C* **2010**, *114*, 9706–9712.

9. Kuo, C. H.; Chen, C. H.; Huang, M. H. *Adv. Func. Mater.* **2007**, *17*, 3773–3780.

10. Somasundaram, S.; Ramannairchenthamarakshan, C.; Detacconi, N.; Rajeshwar, K. *Int. J. Hydrogen Energ.* **2007**, *32*, 4661–4669.

11. Xi, G. C.; Ye, J. H. *Chem. Commun.* **2010**, *46*, 1893–1895.

12. Shang, M.; Wang, W. Z.; Ren, J.; Sun, S. M.; Zhang, L. *Crystengcomm* **2010**, *12*, 1754–1758.

13. Sun, Y. F.; Xie, Y.; Wu, C. Z.; Zhang, S. D.; Jiang, S. S. *Nano Res.* **2010**, *3*, 620–631.

14. Zhang, L.; Chen, D. R.; Jiao, X. L. *J. Phys. Chem. B* **2006**, *110*, 2668–2673.

15. Zhang, Z. J.; Wang, W. Z.; Shang, M.; Yin, W. Z. *Catal. Commun.* **2010**, *11*, 982–986.

16. Zhou, L.; Wang, W. Z.; Zhang, L. S.; Xu, H. L.; Zhu, W. *J. Phys. Chem. C* **2007**, *111*, 13659–13664.

17. Guan, M. L.; Ma, D. K.; Hu, S. W.; Chen, Y. J.; Huang, S. M. *Inorg. Chem.* **2011**, *50*, 800–805.

18. Chatchai, P.; Kishioka, S.-Y.; Murakami, Y.; Nosaka, A. Y.; Nosaka, Y. *Electrochim. Acta* **2010**, *55*, 592–596.

19. Liu, Y.; Chen, L. F.; Hu, J. C.; Li, J. L. Richards, R. *J. Phys. Chem. C* **2010**, *114*, 1641–1645.

20. Murdoch, M.; Waterhouse, G. I. N.; Nadeem, M. A.; Metson, J. B.; Keane, M. A.; Howe, R. F.; Llorca, J.; Idriss, H. *Nature Chem.* **2011**, *3*, 489–492.

21. Lee, M.; Amaratunga, P.; Kim, J.; Lee, D. *J. Phys. Chem. C* **2010**, *114*, 18366–18371.

22. Xiang, Q.; Meng, G. F.; Zhao, H. B.; Zhang, Y.; Li, H.; Ma, W. J.; Xu J. Q. *J. Phys. Chem. C* **2010**, *114*, 2049–2055.

23. Ahmad, M.; Yingying, S.; Nisar, A.; Sun, H. Y.; Shen, W. C.; Wei, M.; Zhu, J. *J. Mater. Chem.* **2011**, *21*, 7723–7729.

24. Sarkar, S.; Makhal, A.; Bora, T.; Baruah, S.; Dutta, J.; Pal, S. K. *Phys. Chem. Chem. Phys.* **2011**, *13*, 12488–12496.

25. Liang, Y. C.; Wang, C. C.; Kei, C. C.; Hsueh, Y. C.; Cho, W. H.; Perng, T. P. *J. Phys. Chem. C* **2011**, *115*, 9498–9502.

26. Gao, S. Y.; Li, Z. D.; Jiang, K.; Zeng, H. B.; Li, L.; Fang, X. S.; Jia, X. X.; Chen, Y. L. *J. Mater. Chem.* **2011**, *21*, 7281–7288.

27. Sun, S. M.; Wang, W. Z.; Zeng, S. Z.; Shang, M.; Zhang, L. *J. Hazard. Mater.* **2010**, *178*, 427–433.

28. Subramanian, V.; Wolf, E. E.; Kamat, P. V. *J. Am. Chem. Soc.* **2004**, *126*, 4943–4950.

29. Wang, Y.; Shen, Y. H.; Xie, A. J.; Li, S. K.; Wang, X. F.; Cai, Y. *J. Phys. Chem. C* **2010**, *114*, 4297–4301.

30. Bao, J.; Chen, W.; Liu, T. T.; Zhu, Y. L.; Jin, P. Y.; Wang, L. Y.; Liu, J. F.; Wei, Y. G.; Li, Y. D. *ACS Nano* **2007**, *1*, 293–298.

31. Tauc, J.; Grigorovici, R.; Vancu, A. *Phys. Stat. Sol.* **1966**, *15*, 627–637.

32. Zheng, Z. K.; Huang, B. B.; Qin, X. Y.; Zhang, X. Y.; Dai, Y.; Whangbo, M. H. *J. Mater. Chem.* **2011**, *21*, 9079–9087.

33. Chen, J. J.; Wu, J. C. S.; Wu, P. C.; Tsai, D. P. *J. Phys. Chem. C* **2011**, *115*, 210–216.

34. Liu, Z. W.; Hou, W. B.; Pavaskar, P.; Aykol, M.; Cronin, S. B. *Nano Lett.* **2011**, *11*, 1111–1116.

35. Ingram, D. B.; Linic, S. *J. Am. Chem. Soc.* **2011**, *133*, 5202–5205.

36. Kohtani, S.; Yoshida, K.; Maekawa, T.; Iwase, A.; Kudo, A.; Miyabe, H.; Nakagaki, R. *Phys. Chem. Chem. Phys.* **2008**, *10*, 2986–2992.

37. Wang, Z. H.; Zhao, S. P.; Zhu, S. Y.; Sun, Y. L.; Fang, M. *Crystengcomm* **2011**, *13*, 2262–2267.

38. Tang, J. W.; Durrant, J. R.; Klug, D. R. *J. Am. Chem. Soc.* **2008**, *130*, 13885-13891.

39. Walsh, A.; Yan, Y. F.; Huda, M. N.; Al-Jassim, M. M.; Wei, S. H. *Chem. Mater.* **2009,** *21*, 547–551.

40. Wu, J. L.; Chen, F. C.; Hsiao, Y. S.; Chien, F. C.; Chen, P. L.; Kuo, C. H.; Huang, M. H.; Hsu, C. S. *ACS Nano* **2011**, *5*, 959-967.

Figures

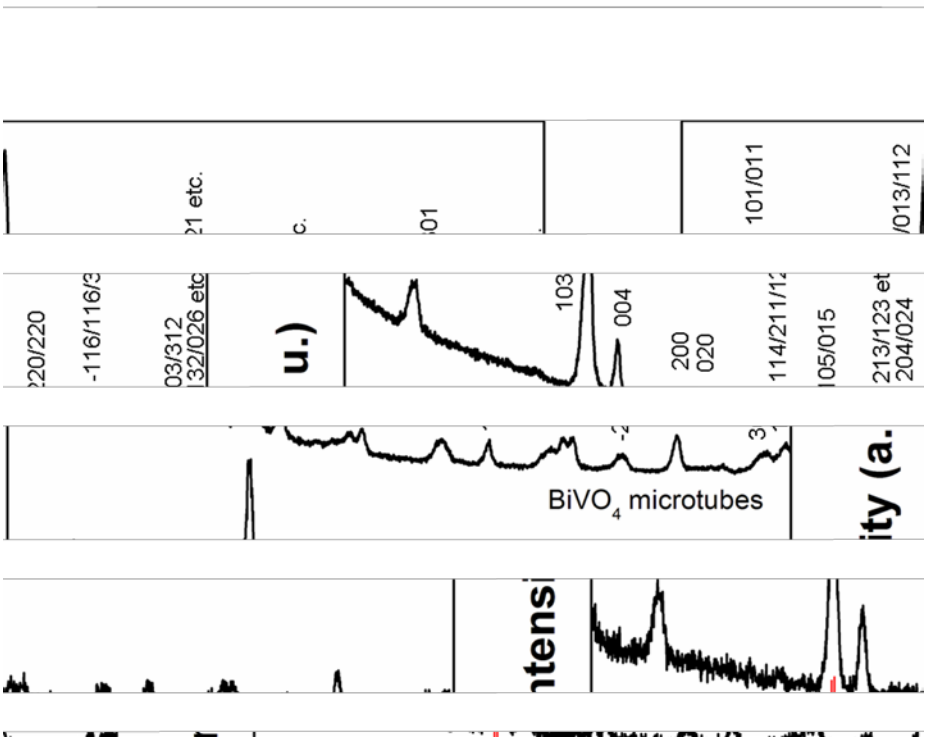

Figure 1. XRD patterns of $BiVO_4$ microtubes and nanosheets. The red lines stand for the standard data (JCPDS No. 83-1699) of monoclinic $BiVO_4$.

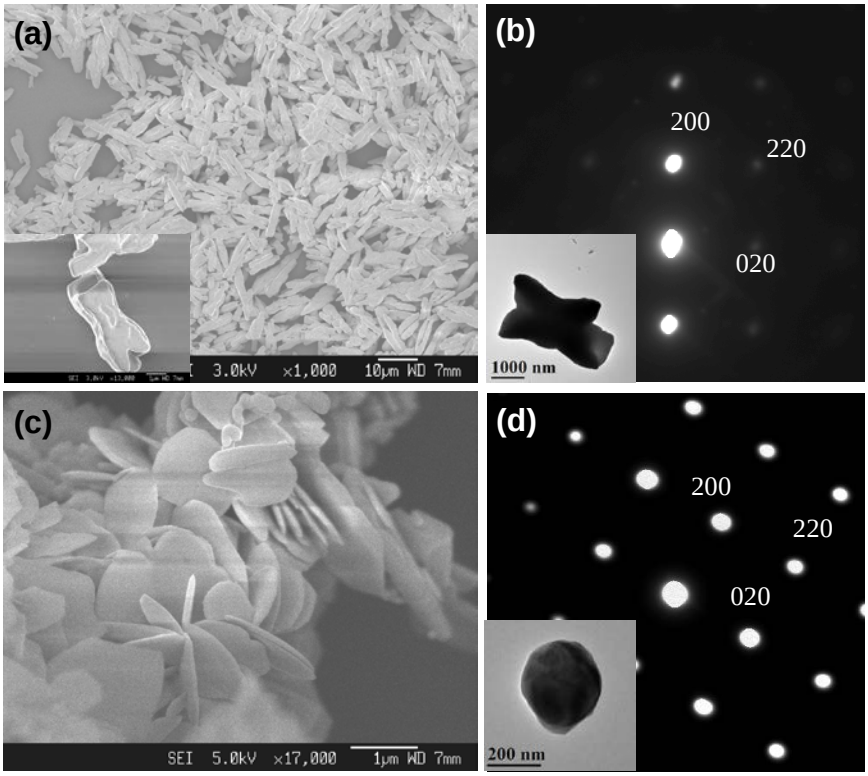

Figure 2. (a) SEM image of $BiVO_4$ microtubes, inset is the zoom-in view of a representative microtube; (b) SAED pattern of a single $BiVO_4$ microtube, inset shows its TEM image; (c) SEM image of $BiVO_4$ nanosheets; (d) SAED pattern of a single $BiVO_4$ nanosheet, inset shows its TEM image.

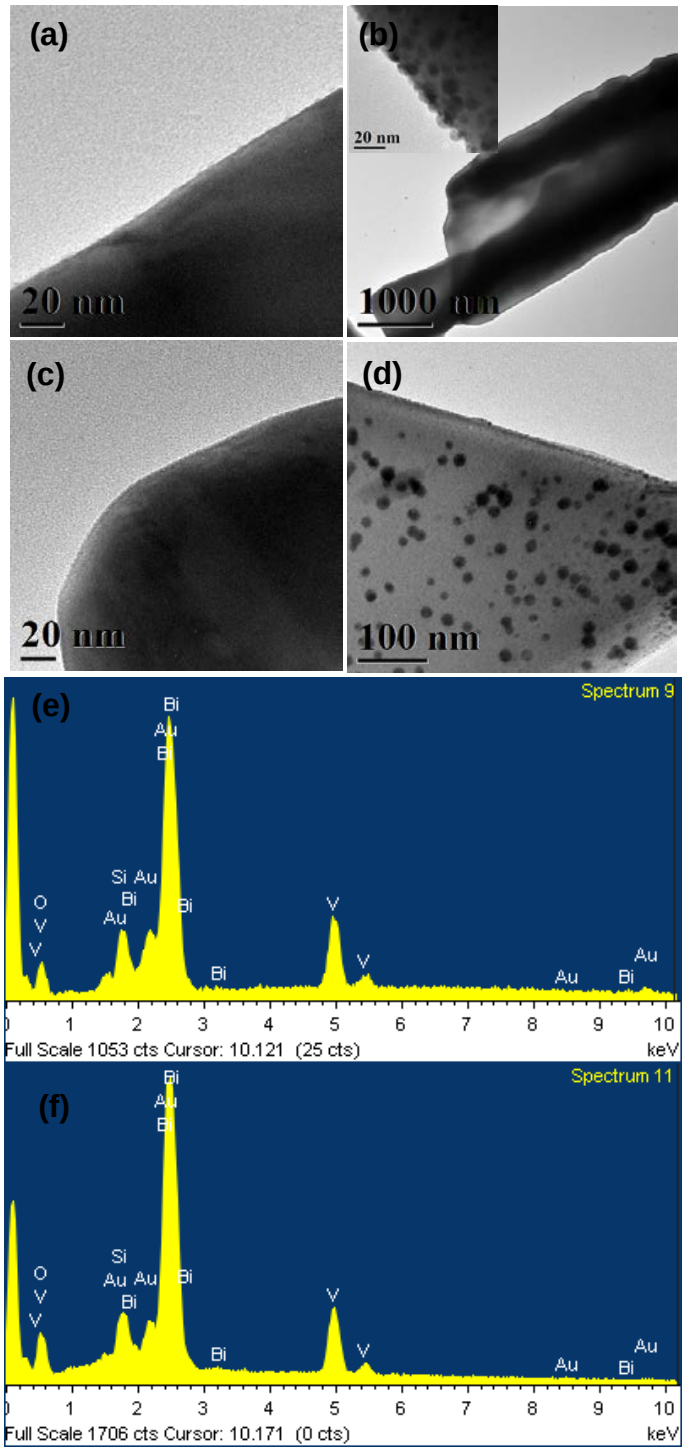

Figure 3. TEM images of the samples: (a) $BiVO_4$ microtubes, (b) Au-$BiVO_4$ microtubes, inset is the edge of a single Au-$BiVO_4$ microtube, (c) $BiVO_4$ nanosheets, and (d) Au-$BiVO_4$ nanosheets. EDX spectra of the samples: (e) Au-$BiVO_4$ microtubes, and (f) Au-$BiVO_4$ nanosheets. The Si peak comes from the silicon substrate.

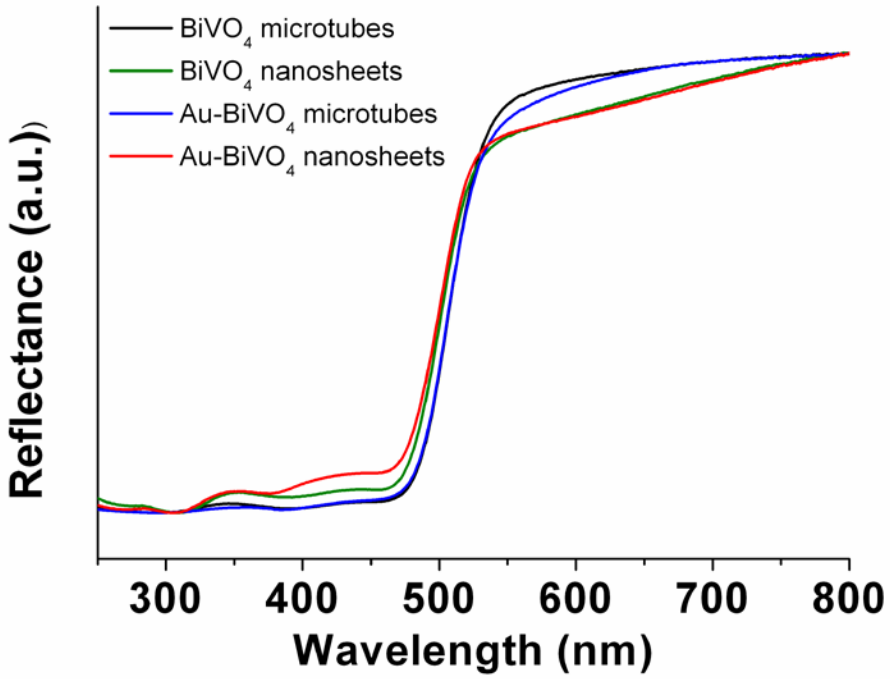

Figure 4. Diffuse reflectance spectra of $BiVO_4$ and Au-$BiVO_4$ structures.

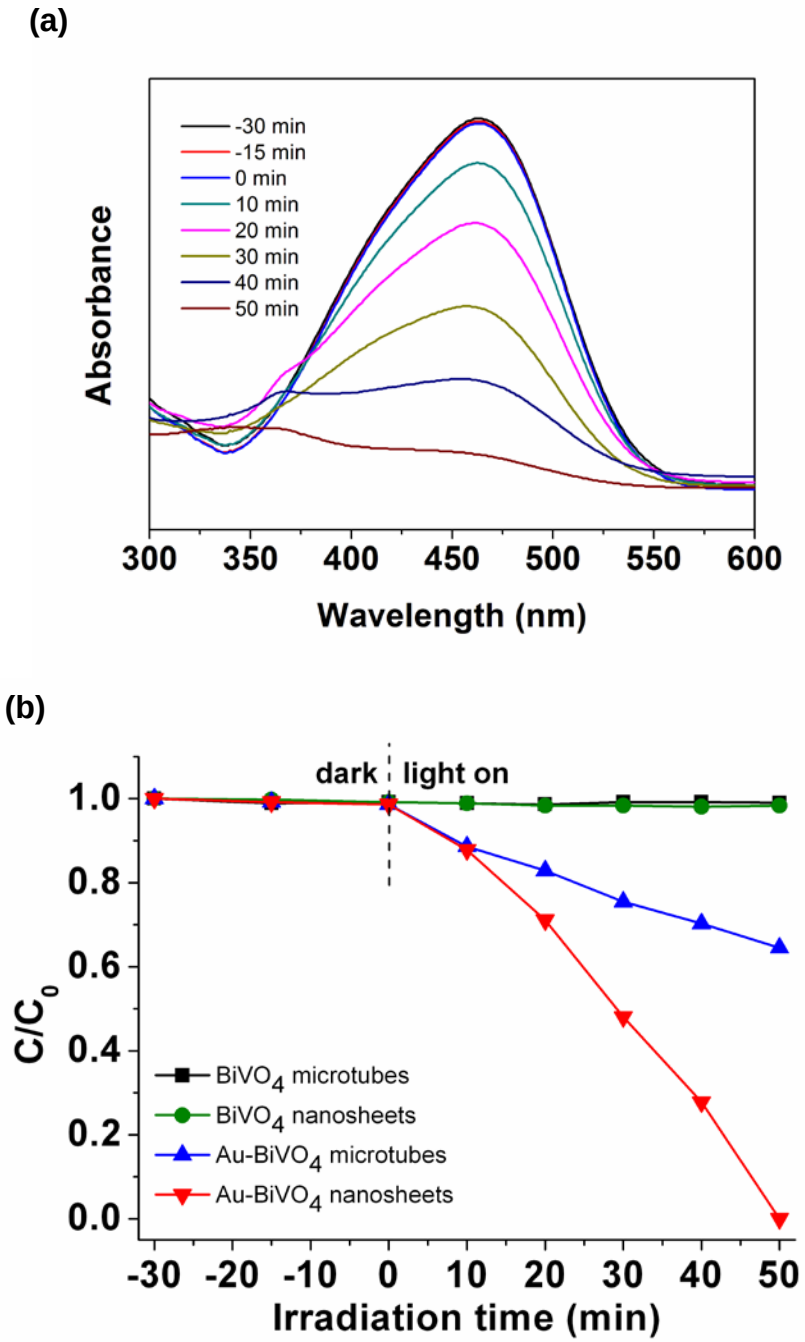

Figure 5. (a) Time-dependent UV-vis absorption spectra of the MO solution in the presence of Au-$BiVO_4$ nanosheets; (b) Photocatalytic degradation ratio of MO versus visible light ($\lambda > 420$ nm) irradiation time by using various photocatalysts.

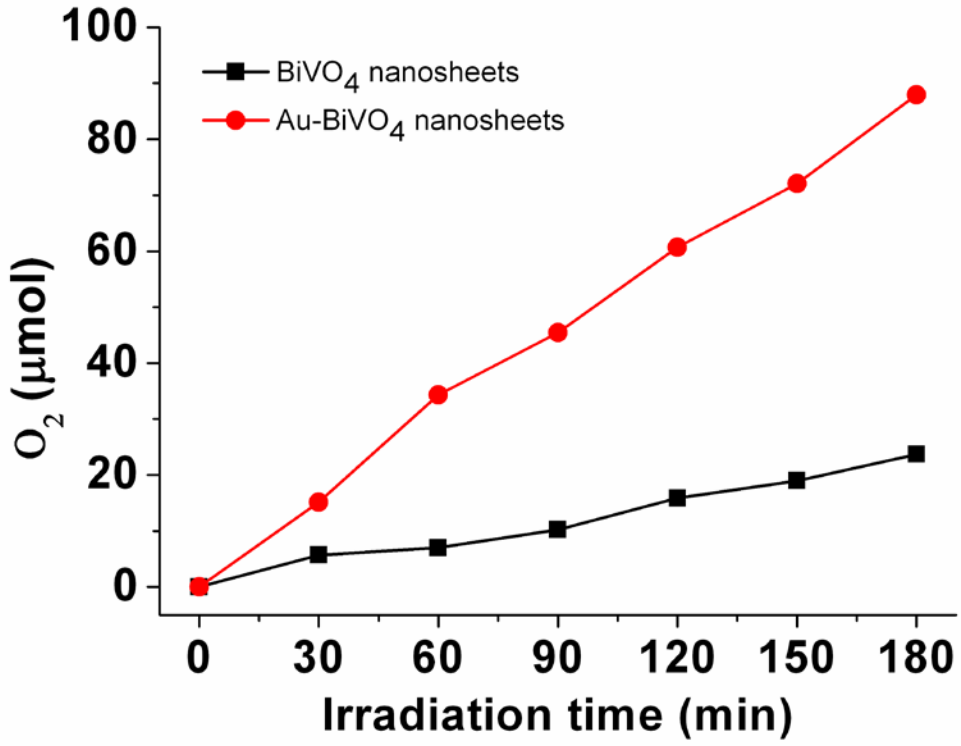

Figure 6. The amount of oxygen evolution versus visible light (λ> 420 nm) time through photocatalytic water oxidation by using $BiVO_4$ and Au-$BiVO_4$ nanosheets.

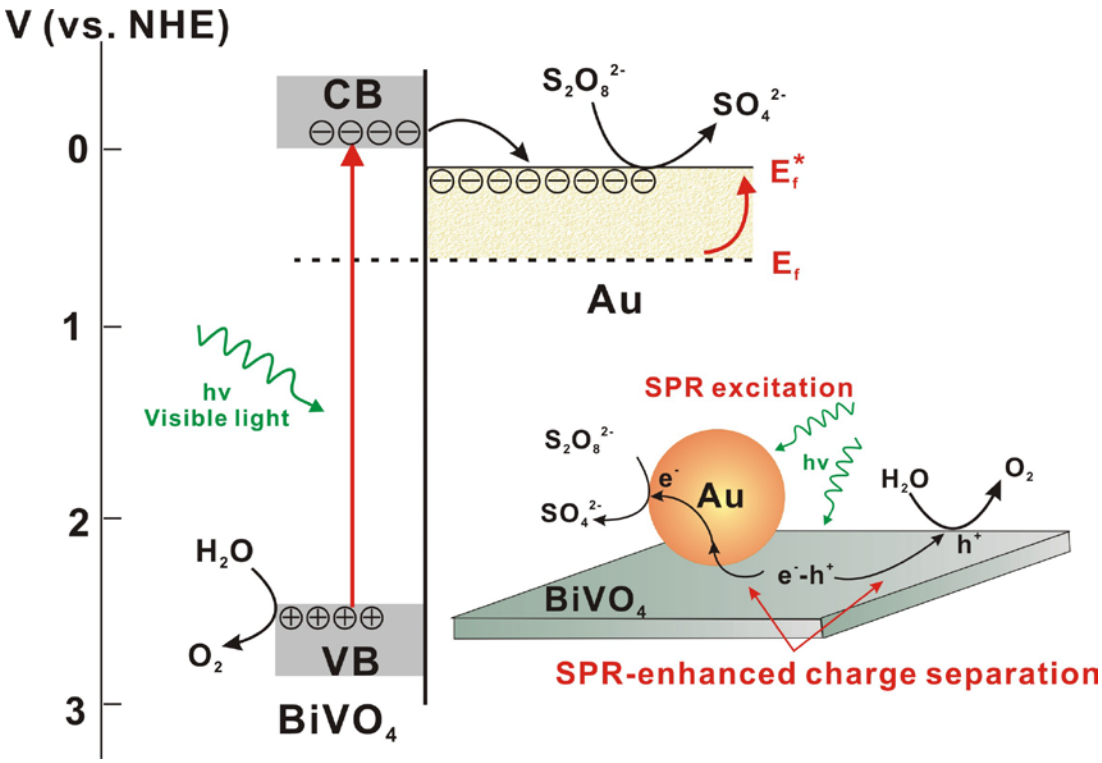

Figure 7. Schematic illustration of the detailed energy alignment in the Au-$BiVO_4$ heterogeneous structure and the proposed mechanism of photocatalytic water oxidation by Au-$BiVO_4$ nanosheets in the presence of sacrificial agent $S_2O_8^{2-}$. The Fermi level (E_f) of Au shifts to more negative potentials (E_f^*) due to the transfer of photogenerated electrons from $BiVO_4$ to Au. The SPR excitation of the gold nanoparticle is believed to enhance electron-hole separation near the Au-$BiVO_4$ hetero-junction.

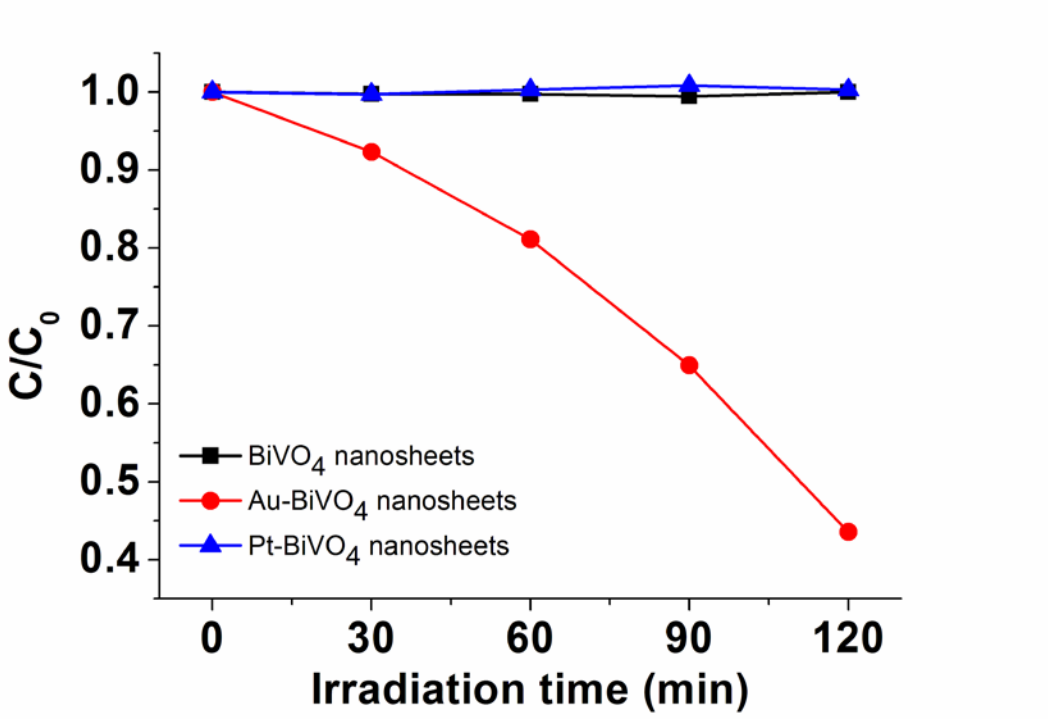

Figure 8. Photocatalytic degradation ratio of MO versus time under irradiation of 500 ± 20 nm light by using Au-$BiVO_4$ nanosheets (red), Pt-$BiVO_4$ nanosheets (blue) and pure $BiVO_4$ nanosheets (black), respectively.

TOC Graphic

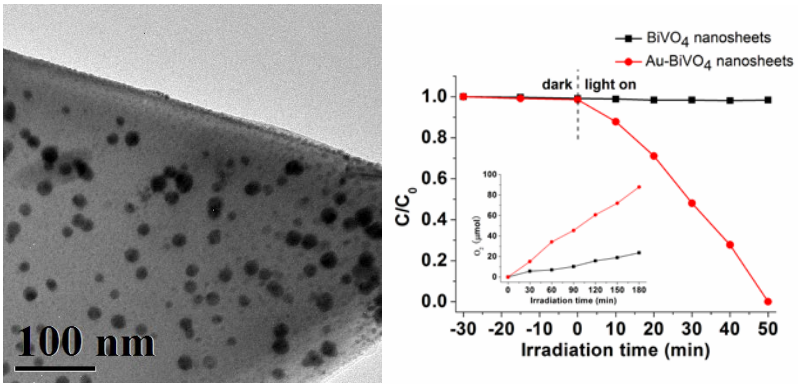

TOC Graphic Legend

Au-$BiVO_4$ heterogeneous nanostructures exhibit highly efficient visible-light photocatalytic activities than pure $BiVO_4$ for both dye degradation and water oxidation.